Journal of
Materials Chemistry A

Materials for energy and sustainability

Accepted Manuscript

This article can be cited before page numbers have been issued, to do this please use: R. Kamar, R. Agoston, G. A. van Riessen, G. Hinsley, A. P. O'Mullane and M. M. W. Jones, *J. Mater. Chem. A*, 2023, DOI: 10.1039/D3TA03923D.

ROYAL SOCIETY OF CHEMISTRY

rsc.li/materials-a

View Article Online
DOI: 10.1039/D3TA03923D

PAPER

Probing the Effect of Metal to Ligand Charge Transfer on the Oxygen Evolution Reaction in Au Incorporated $Co(OH)_2$ Thin Film Electrocatalysts

Received 00th January 20xx,
Accepted 00th January 20xx

DOI: 10.1039/x0xx00000x

Rusha Kamar, [a,b] Roland Agoston, [a] Grant A. van Riessen, [c] Gerard Hinsley, [d] Anthony P. O'Mullane, [a,b] and Michael W. M. Jones *[a,b,e]

First row transition metal oxides have shown potential as affordable catalysts for the oxygen evolution reaction (OER). The addition of small amounts of noble metals such as gold offers significant improvements in catalytic activity while maintaining affordability. However, a fundamental understanding of such enhancement in catalytic activity is still lacking. In this work we correlate Near Edge X-ray Absorption Fine Structure (NEXAFS) data to conventional characterisation techniques to analyse the oxidation state changes that occur during the oxygen evolution reaction in cobalt oxide and cobalt oxide-gold based electrocatalyst thin films to understand their effect on the reaction. We find that the incorporation of gold into the cobalt oxide significantly reduces the ligand to metal charge transfer process on the catalyst surface. We propose that the reduced ligand to metal charge transfer facilitates the formation of the key M-OOH* intermediate (where M is the metal and -OOH* is the ligand) and desorption of O_2 from the catalyst surface, leading to an overall increase in catalyst performance. This study sheds light on how incorporation of small amount of highly electronegative noble metal may have the scope to significantly improve the reactivity of transition metal based thin film catalysts for OER by optimising the ligand to metal charge transfer effect.

1 Introduction

With the ever-intensifying demand for energy, the search for an alternative sustainable source of fuel has become a pressing concern for the future stability of the human race. One potential candidate is hydrogen (H_2), which can be considered as a viable and clean energy source to replace fossil fuels.[1, 2] Several methods are currently available for the industrial production of H_2, for example steam reforming of natural gas, methane pyrolysis, partial oxidation of natural gas or other hydrocarbons, and coal gasification.[3] The production of H_2 from fossil fuels leads to the undesired release of carbon dioxide (CO_2) that contributes to the greenhouse effect[4-6] and is an unviable approach to a sustainable energy economy.[7] Producing hydrogen from water is being investigated extensively due to the potential for this approach to be clean, as the energy input to split water can be sourced from wind and solar. Current methods to produce hydrogen from water such as thermochemical water splitting, direct thermal decomposition, and photocatalytic water splitting have several drawbacks that include high consumption of energy and/or technological difficulty for large-scale production.[8] Electrolysis of water provides an easy, inexpensive, eco-friendly, and efficient way to produce H_2.[9] Water electrolysis involves two chemical half-reactions: the hydrogen evolution reaction (HER) at the cathode and the oxygen evolution reaction (OER) at the anode.[10] There has been a significant amount of research on developing electrocatalysts for both the OER and HER for alkaline electrolysers due to the lower catalyst cost compared to proton exchange membrane electrolysers.[11, 12] However, the OER in particular, limits the overall water splitting rate due to sluggish kinetics associated with the transfer of 4 electrons and the more complex mechanism compared to the HER.[13-15] Noble metal oxides make excellent catalysts for the OER,[16, 17] however, there has been increased effort in developing noble metal-free catalysts to decrease costs and allow for increased production.[18] Transition metals have seen heightened interest, where catalysts have been developed to maximise efficiency and stability and are generally based on oxides of Ni, Fe, Co and Mn.[19-24] Several OER mechanisms have been discussed by Matsumoto and Sato on transition metal oxide catalysts, such as Krasil'shchikov path, the Bockris path and the Yeager's

[a] School of Chemistry and Physics, Queensland University of Technology (QUT), Brisbane, Queensland, Australia.
[b] Centre of Materials Science, Queensland University of Technology (QUT), Brisbane, Queensland, Australia.
[c] Department of Mathematical and Physical Sciences, School of Computing, Engineering and Mathematical Science, La Trobe University, Bundoora, Victoria 3086, Australia.
[d] Deutsches Elektronen Synchrotron DESY
[e] Central Analytical Research Facility (CARF), Queensland University of Technology (QUT), Brisbane, Queensland, Australia

Electronic Supplementary Information (ESI) available: [Additional experimental details, XRD patterns, XPS survey scans, ECSA measurements]. See DOI: 10.1039/x0xx00000x

path.[25] In alkaline electrolyte all reaction pathways start with the adsorption of hydroxide on the active sites followed by oxidation of -OH* and -O* to -OOH* which is generally regarded as the active form of many catalysts, where * denotes intermediate ligands. Indeed, many transition metal-based catalysts, even those based on chalcogenides and phosphides, ultimately convert into M-OOH* species at the surface of the catalyst prior to the OER.[26-28] Among the most studied transition metal-based catalysts, those containing cobalt show significant promise for the OER.[29-32] The activity of the transition metal oxide catalysts for the OER can be improved upon further by the incorporation of noble metals such as Au, which has been reported to enhance the performance of $Co(OH)_2$,[33-35] cobalt nanosheets,[36] Co_3O_4[37-39] and Ni-Fe based systems. [40] It has been hypothesised that the increased activity is due to electronic interactions between Au and the metal oxides/hydroxides that perturbs the oxidation state of Co. The high electronegativity of Au has been shown to facilitate formation of Co^{4+} in amorphous $Co(OH)_2$ films.[33] A core-shell structure of Co_3O_4 nanocrystals (NCs) developed on an Au core enhanced the OER activity of the Co_3O_4 NCs 7 times more than a mixture of Au and Co_3O_4 NCs which is likely due to a strong synergistic effect between the core and the shell.[37] An Au incorporated $Co(OH)_2$ micro-clustered electrocatalyst was reported to show better OER performance compared to $Co(OH)_2$ by lowering the binding energy of intermediates on $Co(OH)_2$-Au where the Au acted as an electron sink for the oxidation of Co^{2+} and Co^{3+} to Co^{4+}.[35] However, further research is required to understand the exact role that Au plays in these systems. In this work we investigate $Co(OH)_2$ and $Co(OH)_2$-Au materials to determine the influence of Au on the OER under alkaline conditions. We correlate Near Edge X-ray Absorption Fine Structure (NEXAFS) data to conventional characterisation techniques to understand the chemical changes that occur at the surface of both Au-free, and Au-incorporated $Co(OH)_2$ thin film electrocatalysts and how this impacts their OER performances.

2 Experimental

2.1 Preparation of Co-based thin films

Pristine and Au-incorporated $Co(OH)_2$ electrocatalyst films were prepared as working electrodes on three different substrates: Pt-coated silicon nitride windows, glassy carbon (GC) electrode and a Pt-coated silicon wafer (Table S1). The Pt-coated silicon nitride substrates were used to prepare samples for NEXAFS data collection, while a GC electrode with 3 mm diameter was used to measure the electrocatalytic performance of the prepared electrocatalyst. The Pt-coated silicon wafer was used to electrodeposit films for pre-characterisation using scanning electron microscopy (SEM), energy dispersive X-ray spectroscopy (EDX), transmission electron microscopy (TEM) and X-ray photon spectroscopy (XPS). All films were prepared under ambient conditions at a temperature of 18°C. Silicon nitride windows were first coated with 2 nm thick adhesion layer of titanium followed by a 10 nm thick platinum coating via electron-beam physical vapour deposition to improve conductivity of the substrate. A standard 3-electrode system consisting of an Ag/AgCl reference and Pt wire counter electrode was used for electrochemical experiments. $Co(OH)_2$ was electrodeposited from a 10 mM solution of $Co(NO_3)_2$ by chronoamperometry (CA). $Co(OH)_2$ incorporated with Au was similarly electrodeposited from a solution of 10 mM $Co(NO_3)_2$ and 1 mM $KAuBr_4$. An Au film was also deposited on a GC electrode and the Pt-coated silicon wafer from a 1mM $KAuBr_4$ solution. The potential applied for each electrodeposition was -1.05 V (vs. Ag/AgCl) for 60 s following previous literature.[34] The resulting Co oxide film thickness was approximately equal to a few microns. These films were subjected to OER in 0.1 M NaOH at 0.75 V (vs. Ag/AgCl) for 4 h. Small bubbles of O_2 were observed during the reaction on the film surface and inside the solution (Figure S4). Cyclic voltammograms (CV) for $Co(OH)_2$ and $Co(OH)_2$-Au films were recorded between a range of 0.9 – 1.66 V (vs RHE) at a sweep rate of 20 mV s^{-1} in 0.1 M NaOH to measure their electrochemical performance. (See supporting information for further details.)

2.2 Surface characterisation

SEM and EDX were performed using a Zeiss Sigma FESEM with an accelerating voltage of 5.0 keV and 30 keV respectively. TEM images were taken using a JEOL 2100 instrument at 200 kV. X-ray photoelectron spectroscopy measurements were carried out on an AXIS Supra instrument (Kratos Analytical, UK). All the measurements were done using the charge neutraliser as a default. Atomic compositions for all the elements were calculated using the CasaXPS software.

NEXAFS spectra of the prepared pre- and post-OER samples were collected at the SXR beamline at the Australian Synchrotron.[41] The films were electrodeposited on silicon nitride windows that were mounted on a stainless-steel sample holder using a double-sided carbon tape. The base pressure in the system was $5x10^{-10}$ Torr. Co L edge data were collected at 55° incidence angle over the energy range of 770 eV to 820 eV using an energy step of 0.1 eV acquiring 500 data points. A reference sample of Co foil was placed upstream and simultaneously measured to provide a standard for the X-ray energy reference for the scans with the L3 peak calibrated to 778.6 eV. Two detection modes: Auger Electron Yield (AEY) and Total Fluorescent Yield (TFY) were used to acquire the absorption signal by using a hemispherical electron analyser and retarding grid analyser, respectively. The signal is more bulk sensitive in TFY compared to AEY due to the greater escape depth of the fluorescent X-rays compared to electrons. The data were normalised with respect to the incident photon flux monitored using a gold mesh with high transmissivity placed upstream of the sample. A linear background fitted to the pre-edge region was subtracted from the spectra.

3 Results and discussion

Cyclic voltammetry was used to investigate the effect of Au within an electrodeposited $Co(OH)_2$ film on the OER, which is shown in Figure 1. The $Co(OH)_2$-Au sample shows a significant

reduction in the onset potential to 1.45 V compared to 1.55 V for $Co(OH)_2$. The current density is also significantly higher over the potential range of 1.45 V until the end of the sweep at 1.66 V. Both samples were briefly tested for stability with little change in activity of both films over 10 cycles (Figure 1a). A control electrodeposited Au sample was also tested which is essentially inactive for the OER in the potential range of study. The Tafel plot presented in Figure 1b shows tafel slope values of 79 and 87 mV dec^{-1} for $Co(OH)_2$-Au and $Co(OH)_2$, respectively. This indicates improved electron transfer kinetics at $Co(OH)_2$-Au but no change in the rate-determining step. In addition, the electrochemical surface area (ECSA) of the $Co(OH)_2$-Au film was found to be smaller than that of the $Co(OH)_2$ film (Figure S3, Table S2) which means that the enhanced activity of the Au incorporated film must be from a different phenomenon other than an increased active surface. To understand why the presence of Au is improving efficiency of the OER both catalysts were extensively characterised before and after continuous electrolysis for 4 h at a potential of 1.75 V vs RHE.

Characterisation after the OER was undertaken as it is now well established that transition metal oxide/hydroxide catalysts can change quite significantly both in terms of their morphology and chemical composition.[28, 34, 42] The as-deposited $Co(OH)_2$ film shows a flake-like morphology associated with metal hydroxide films and a uniform distribution of Co and O throughout the film (Figure 2a). After OER the film appears slightly rougher but largely the morphology remains constant (Figure 2b). For $Co(OH)_2$-Au the presence of Au produces a significantly smoother morphology (Figure 2c). EDX mapping shows Au is deposited as clusters across the film, where the size of the Au clusters varies from 5-15 nm. After the OER, the film morphology changes significantly with a large increase in the fine-grained coarseness of the film. The presence of gold is still maintained in the film in similar clusters (Figure 2d). This increased general film roughness would partially explain the increase in OER current density seen for the $Co(OH)_2$-Au sample due to greater accessibility to active sites, however, it would not explain the significant change in onset potential, indicating that this is not purely a surface area effect as also indicated by the ECSA measurements. Further morphological investigation of the as-deposited $Co(OH)_2$ film by TEM shows sheet like structure (Figure 3a) with a d spacing of 2.55Å which is in accordance with the α-$Co(OH)_2$ (012) plane.[43] After the OER the film shows some agglomeration where the lattice spacing increases to 3.05Å (Figure 3b). This is consistent with the Co_3O_4 (220) crystalline plane.[44] Elsewhere, sheet structures are observed (Figure 3b) where the lattice spacing is 2.2Å. In the TEM image of the $Co(OH)_2$-Au film, Au spots are clearly visible on the sheet nanostructures (Figure 3c). Here, the lattice spacing is 3.12 Å indicating the formation of Co_3O_4 and the presence of the (220) plane[44] while lattice fringe spacings for Au are measured at 2.32Å consistent with the (111) plane[45]. The structure of the cobalt oxide around the Au spots is amorphous in the $Co(OH)_2$-Au film compared to the structure in the Au free zones in the same film, where crystalline regions are observed more easily. After the OER the morphology remains essentially the same as the as-deposited $Co(OH)_2$-Au film (Figure 3d), but both Co oxide and Au crystalline regions can be found in the same vicinity. After the OER the lattice spacing in the film is 2.32 Å which is attributed to the Co_3O_4 (222) plane[46] while for the Au particle it remains at 2.37 Å for Au (111). This interfacial region between Au and Co_3O_4 may be responsible for increased activity given recent reports on the importance of heterojunctions in electrocatalyst films for the OER.[24, 47, 48] The presence of gold was also confirmed by XRD analysis shown in Figure S1.[45] No distinct peaks due to either $Co(OH)_2$ or Co_3O_4 were found for the as deposited or post OER films suggesting that the crystalline regions are not extensive within the electrodeposited films. While the TEM analysis indicates the presence of both crystalline and amorphous phases of various cobalt oxides on the films, further investigation is required to confirm their oxidation states and the effect of Au on them to explain the enhanced activity of the $Co(OH)_2$-Au film.

To determine the influence of surface chemistry, XPS characterisation was undertaken (Figure 4). The XPS survey scan is also provided in Figure S2 showing the presence of Co, O and Au as expected. For $Co(OH)_2$ the Co XPS spectrum has a peak at 780.2 eV due to Co $2p_{3/2}$ which is in accordance with $Co(OH)_2$ representing the Co^{2+} state (Figure 3a).[49] This peak is slightly shifted to lower binding energy to 779.6 in the $Co(OH)_2$ post-OER sample (Figure 4c) while another peak at 782.0 eV in the pre-OER sample also shifted to a lower binding energy of 781.1 eV in the post OER sample (Figure 3a and 3c). This chemical shift distinguishes the divalent oxide in the post sample from its hydroxide in the pre- sample, [49] and indicates the formation of Co_3O_4 or CoOOH species. The suppression of the peak at 785.5 eV and appearance of the peak at 789.1 eV after the OER (Figure 3c) is also indicative of Co_3O_4 or CoOOH formation.[34]

For the O 1s XPS spectra the O 1s spectrum in the $Co(OH)_2$ sample is comprised of three peaks (Figure 3b) in the pre-OER sample and four peaks in the post OER sample (Figure 3d). The main peak in the pre sample is at 531.2 eV which is the O from the hydroxyl group. [49] In the post OER sample two peaks at the lower range from 528-529 eV and the main peak at 531.1 eV indicate the presence of lattice oxide ions O^{2-}.[49] The intensities of oxide and hydroxyl peaks are very close in the post-OER film, indicating that CoOOH is starting to form at this stage of the reaction. In addition, oxygen from adsorbed H_2O can be seen in both samples near 532.5 eV.

For $Co(OH)_2$-Au the Co $2p_{3/2}$, O 1s and Au 4f XPS spectra for the pre- and post-OER samples are shown in Figure 3f-h and 3i-k, respectively. For the Co $2p_{3/2}$ spectrum, similar changes occur after the OER when compared to $Co(OH)_2$, therefore the presence of Au is not influencing this transformation of $Co(OH)_2$ into higher oxidation Co species such as Co_3O_4 (as seen from TEM analysis) or CoOOH. Likewise, the O 1s spectra are similar both before and after the OER when compared to $Co(OH)_2$, where the only difference is the presence of small amount of lattice oxides in the pre-OER sample. The Au 4f spectra (Figure 4h and 4k) is in accordance with the presence of Au^0 with two main peaks at around 84.4 and 87.9 eV.[50] Interestingly oxidation of Au is not observed after the OER, indicating that Au is most likely present below a surface layer of $Co(OH)_2$. When the Au 4f

spectrum from an electrodeposited Au film (no $Co(OH)_2$) is compared with the pre-OER Au 4f spectrum, a shift to lower binding energy is observed in the $Co(OH)_2$-Au pre-OER sample (Figure 4e). This indicates an electronic shift in the film as Au acts as an electron sink when $Co(OH)_2$ is present. From the XPS analysis, the presence of Au does not extensively influence the surface chemistry of the film which in both cases results in a cobalt oxide/hydroxide containing Co in a higher oxidation state than the initial $Co(OH)_2$ film. Therefore, the origin of the shift in onset potential for the OER and significantly increased current density is likely due to another phenomenon. Previous work[34, 38] has indicated that the electronegativity of Au promotes Co^{4+} formation, which is responsible for increased OER activity, however the cyclic voltammogram in Figure 1a does not indicate that this process has occurred (no observation of an obvious redox peak prior to the onset of the OER) while the XPS data indicates that the changes in surface oxidation states are comparable between $Co(OH)_2$ and $Co(OH)_2$-Au and that the addition of Au does not promote Co^{4+} formation.

To investigate potential interactions occurring between Au and $Co(OH)_2$ that are not observable by XPS, NEXAFS spectra of the pre- and post-OER samples were collected in AEY and TFY modes at the SXR beamline at the Australian Synchrotron.[41] The L edge spectra of Co are separated into two regions; L2 and L3 that originate from the 2p core hole spin-orbital coupling[51] (Figure 5a). The absorption peaks originate from the dipole transitions between the core 2p level and unoccupied 3d states. The two levels have Coulomb interactions that are governed by the local electronic structure.[52, 53] The spectrum shows a multiplet peak starting at 777 eV followed by two subpeaks (peaks 1, 2 and 3), another peak at 780 eV (peak 4) while a shoulder is observed at 782.5 (peak 5). The multiplet peaks 1, 2, and 3 originate from the electronic transition associated with the Co^{2+} site symmetry in the crystal structure of $Co(OH)_2$.[54] The peak splits into four sub-points due to geometrical distortion of the crystal structure of charge neutral interspacing layers between two different layers of the crystal lattice.[54] The peaks obtained in both pre-OER samples of $Co(OH)_2$ and $Co(OH)_2$-Au match the NEXAFS peaks of Co^{2+} O_h symmetry[54] while similar peaks are observed in the TFY spectra (Figure 6a) divided into the two regions L2 and L3.

When the NEXAFS spectra of $Co(OH)_2$ before and after the OER are compared, stark differences can be seen (Figure 5c). The post-OER spectrum has shifted to higher energy, indicating a shift to a higher valency/oxidation state which is in accordance with the XPS data.[55] In addition, peak 4 intensifies significantly compared to peak 2 and peak 3 and a sharper peak 6 is observed in the post OER spectrum. These features of the $Co(OH)_2$ post OER sample match with the HS-CoO+LS-$EuCoO_3$ scenario (HS: high spin, LS: low spin) described by Chang *et al*.[56], denoting a mixture of high spin and low spin states (intermediate spin state) configurations, while the dominant peak 4 in this spectrum indicates Co^{3+} in the cobalt structure.[57]

Two satellite peaks (peak 7 and peak 8) can be seen at 784.5 eV and 799.5 eV respectively, and originate from a metal-to-ligand charge transfer (MLCT) to unoccupied ligand orbitals involved in π back-bonding to the Co site,[58] which has been reported in other systems.[59]

Similar changes can be seen when the NEXAFS spectra of $Co(OH)_2$-Au pre- and post-OER samples are compared (Figure 5d), but the charge transfer peaks (peaks 7 and 8) are less prominent in the $Co(OH)_2$-Au post OER sample spectrum (Figure 5b), indicating that the addition of Au results in a lower MLCT to unoccupied ligand orbitals. We suggest that this is due to the more electronegative Au pulling the shared electrons involved in the π back-bonding between the Co metal and unoccupied ligand orbitals, thus reducing the charge transfer effects. This can be seen more clearly in Figure 5b where peak 7 and peak 8 are sharper in the $Co(OH)_2$ post OER sample than in the $Co(OH)_2$-Au post OER sample. When the AEY and TFY spectra are compared against the dominant characteristic peak 4 in the $Co(OH)_2$ post OER samples (Figure 6c) it can be seen from the relative peak intensity ratios between peak 7 and peak 4, that the satellite peaks are sharper in the AEY spectrum than in TFY spectrum (0.44 in $Co(OH)_2$ AEY, 0.31 in $Co(OH)_2$ TFY). As AEY is more surface sensitive than TFY (only measuring the top few nm) these results indicate that the charge transfer effect is more dominant at the surface.[60] The same trend is also noticed in the $Co(OH)_2$-Au post OER sample (Figure 6b) (relative peak intensity ratios between peak 7 and peak 4 are: 0.34 in $Co(OH)_2$-Au AEY and 0.23 in $Co(OH)_2$-Au TFY). We suggest that this limited charge transfer effect leads to the enhanced performance of the $Co(OH)_2$-Au thin films for the OER. The general mechanism is believed to be the following:[38]

$$M + OH^- \rightarrow M\text{-}OH^* + e^- \quad (1)$$

$$OH^- + M\text{-}OH^* \rightarrow H_2O + M\text{-}O^* + e^- \quad (2)$$

$$M\text{-}O^* + OH^- \rightarrow M\text{-}OOH^* + e^- \quad (3)$$

$$M\text{-}OOH^* + OH^- \rightarrow M\text{-}O_2 + H_2O + e \quad (4)$$

$$M\text{-}O_2 \rightarrow M + O_2 \quad (5)$$

where M refers to the metal, in this case Co and -OH*, -O*, -OOH* are intermediate ligands.

It has been reported that the Co cations in the electrocatalyst reach higher oxidation states during the earlier steps of OER (eqns. 1-3) but need to convert back to lower oxidation states for the final desorption process of O_2 from the catalyst surface (eqn. 5).[37, 61] The presence of Au reduces the charge transfer between the ligand and the metal cations enabling this conversion of Co ions to lower oxidation states and easier desorption of O_2 thereby leading to an overall increase in catalyst efficiency. In addition, if less MLCT occurs then the electrophilicity of the adsorbed O that is formed early in the reaction (eqns. 1-2) is enhanced which would facilitate the formation of O-OH via nucleophilic attack by an OH^- anion (eqn. 3). The process described in eqn. 3 is the rate determining step for the OER.[38] Therefore, the presence of Au appears to directly effect this rate determining step resulting in enhanced OER catalysis.

The schematics in Figure 7 outlines the metal to ligand charge transfer effect in Au incorporated and Au free thin films of

Journal of Material Chemistry A PAPER

DOI: 10.1039/D3TA03923D

$Co(OH)_2$ based electrocatalysts. The highly electronegative Au in the $Co(OH)_2$-Au sample pulls the shared electron in the π back bonding between the metal and the ligands facilitating the nucleophilic attack of the OH^- ions from the alkaline medium on the adsorbed oxygen which then results in desorption of an oxygen molecule from the catalyst surface. This also leads to the conversion of higher valency Co back to a lower valency for the reaction to continue. In the Au free catalyst, no such electron pull is felt by the shared π back bonding electrons between the metal and ligands leading to a higher MLCT process and increased electron density around the adsorbed oxygen on the catalyst surface which reduces its reaction with hydroxyl ions via eqn. 3. Hence, we observe increased current density indicating more oxygen formation at the anode in the $Co(OH)_2$-Au system.

Previous work on a soft X-ray absorption spectroscopy study of the O K-edge in a Ni-Fe(O_xH_y) electrocatalyst for the OER revealed formation of electron-deficient oxygen sites, highly electrophilic in nature, that appear and disappear in relation to the transformation process of $Ni^{2+} \rightarrow Ni_{3+/4+} \rightarrow Ni^{2+}$, and facilitate nucleophilic attack, although no MLCT satellites peaks were observed in the NEXAFS of Ni or Fe L-edge spectra.[62] In another study, a Ni oxide monolayer on Au electrode showed higher OER activity compared to the OER performances of β-NiOOH and γ-NiOOH on Ni electrodes.[63] The enhanced OER activity was attributed to the charge transfer effect from the oxide to the highly electronegative Au, resulting in the potential formation of a mixed Ni/Au oxide, which was supported by in situ Raman and ex-situ XPS studies.[63] In a NEXAFS study of Mn L-edge spectra of an Au supported nanoparticulate MnO_x catalyst for the OER, it showed enhanced OER activity compared to pure MnO_x where interfacial or local effect of Au favoured formation of less oxidised MnO_x, however no MLCT effects were explored.[64] These studies indicate that there may be scope for further X-ray absorption spectroscopy studies of these systems to explore the effects of charge transfer in the presence of Au.

Conclusions

Au-incorporated, and Au-free $Co(OH)_2$ based thin films were compared as electrocatalysts for the OER under alkaline conditions where it was found that the presence of Au resulted in significant enhancement in OER performance which was not due to increased surface area. XPS analysis revealed that $Co(OH)_2$ in the absence and presence of Au resulted in similar surface chemistry after the OER, namely the formation of Co_3O_4 and CoOOH. However, TEM analysis revealed the formation of crystalline regions of Co_3O_4 around the Au particles which may contribute to enhanced activity. NEXAFS analysis illustrated a reduced charge transfer effect between the oxygen ligand and Co cations due to the high electronegativity of Au in the film. This phenomenon increases the electrophilicity of the adsorbed oxygen of the M-O* intermediate on the catalyst surface that allows for nucleophilic attack of hydroxyl ions to form the key reactive M-OOH* species which then proceeds to form adsorbed O_2 and ultimately its evolution from the surface. This study encourages further investigation using NEXAFS on other electrocatalytic reactions where the presence of an MLCT process could be an influencing factor.

Author Contributions

Rusha Kamar: writing, editing, investigation, methodology, characterisation, data acquisition. Anthony P. O'Mullane: Editing, project management, supervision, funding acquisition, data acquisition. Roland Agoston: Methodology, visualisation. Grant A. van Riessen: editing, data acquisition. Gerard Hinsley: Data acquisition. Michael W. M. Jones: Supervision, funding acquisition, data acquisition, editing, project management.

Conflicts of interest

There are no conflicts to declare.

Acknowledgements

This research made use of the equipment and personnel at Central Analytical Research Facility (CARF), QUT. This research was undertaken on the SXR beamline at the Australian Synchrotron, part of ANSTO. Anthony P. O'Mullane gratefully acknowledges the ARC (DP180102869) for funding. Also, many thanks to Blair Haydon and Jerome Knappett for their assistance during data acquisition at the Australian Synchrotron.

Notes and references

1. E. Hu, Y. Feng, J. Nai, D. Zhao, Y. Hu and X. W. D. Lou, *Energy & Environmental Science*, 2018, **11**, 872-880.
2. F. Yu, H. Zhou, Y. Huang, J. Sun, F. Qin, J. Bao, W. A. Goddard, S. Chen and Z. Ren, *Nature communications*, 2018, **9**, 1-9.
3. C. M. Kalamaras and A. M. Efstathiou, *Conference papers in science*, 2013, 2-4.
4. B. You and Y. Sun, *Accounts of chemical research*, 2018, **51**, 1571-1580.
5. W. Wang, M. Xu, X. Xu, W. Zhou and Z. Shao, *Angewandte Chemie International Edition*, 2020, **59**, 136-152.
6. K. Oka, O. Tsujimura, T. Suga, H. Nishide and B. Winther-Jensen, *Energy & Environmental Science*, 2018, **11**, 1335-1342.
7. J. G. Love, A. P. O'Mullane, F. A. Boulaire and I. D. R. Mackinnon, *Sustainable Energy & Fuels*, 2022, **6**, 4008-4023.
8. P. Nikolaidis and A. Poullikkas, *Renewable and sustainable energy reviews*, 2017, **67**, 597-611.
9. S. Sebbahi, N. Nabil, A. Alaoui-Belghiti, S. Laasri, S. Rachidi and A. Hajjaji, *Materials Today: Proceedings*, 2022, **66**, 140-145.
10. I. Roger, M. A. Shipman and M. D. Symes, *Nature Reviews Chemistry*, 2017, **1**, 1-13.
11. R. R. Raja Sulaiman, W. Y. Wong and K. S. Loh, *International Journal of Energy Research*, 2022, **46**, 2241-2276.
12. Q. Zhou, L. Liao, H. Zhou, D. Li, D. Tang and F. Yu, *Materials Today Physics*, 2022, **26**, 100727.

13. Y. Zhang, Q. Fu, B. Song and P. Xu, *Accounts of Materials Research*, 2022, **3**, 1088-1100.
14. C. S. Rout and D. J. Late, *Fundamentals and Supercapacitor Applications of 2D Materials*, Elsevier, 2021.
15. A. J. Wain and E. J. Dickinson, *Nanoscale Electrochemistry*, Elsevier, 2021.
16. H. Kim, T. Y. Yoo, M. S. Bootharaju, J. H. Kim, D. Y. Chung and T. Hyeon, *Advanced Science*, 2022, **9**, 2104054.
17. Q. Shi, C. Zhu, D. Du and Y. Lin, *Chemical Society Reviews*, 2019, **48**, 3181-3192.
18. F. Lyu, Q. Wang, S. M. Choi and Y. Yin, *Small*, 2019, **15**, 1804201.
19. M.-I. Jamesh and M. Harb, *Journal of Energy Chemistry*, 2021, **56**, 299-342.
20. Y.-C. Zhang, C. Han, J. Gao, L. Pan, J. Wu, X.-D. Zhu and J.-J. Zou, *ACS Catalysis*, 2021, **11**, 12485-12509.
21. C. Feng, M. B. Faheem, J. Fu, Y. Xiao, C. Li and Y. Li, *ACS Catalysis*, 2020, DOI: 10.1021/acscatal.9b05445.
22. M. Yin, H. Miao, R. Hu, Z. Sun and H. Li, *J. Power Sources*, 2021, **494**, 229779.
23. R. Agoston, M. Abu Sayeed, M. W. M. Jones, M. D. de Jonge and A. P. O'Mullane, *Analyst*, 2019, **144**, 7318-7325.
24. A. P. O'Mullane, *Journal of Physics: Energy*, 2020, **2**, 041001.
25. Y. Matsumoto and E. Sato, *Materials chemistry and physics*, 1986, **14**, 397-426.
26. W. Li, D. Xiong, X. Gao and L. Liu, *Chemical Communications*, 2019, **55**, 8744-8763.
27. B. R. Wygant, K. Kawashima and C. B. Mullins, *ACS Energy Letters*, 2018, **3**, 2956-2966.
28. U. K. Sultana and A. P. O'Mullane, *ChemElectroChem*, 2019, **6**, 2630-2637.
29. Y. Wang, C. Xie, D. Liu, X. Huang, J. Huo and S. Wang, *ACS applied materials & interfaces*, 2016, **8**, 18652-18657.
30. Z. Liu, H. Tan, D. Liu, X. Liu, J. Xin, J. Xie, M. Zhao, L. Song, L. Dai and H. Liu, *Advanced Science*, 2019, **6**, 1801829.
31. S. A. Khalate, S. A. Kadam, Y.-R. Ma, S. S. Pujari and U. M. Patil, *Journal of Alloys and Compounds*, 2021, **885**, 160914.
32. B. Bayatsarmadi, Y. Zheng, V. Russo, L. Ge, C. S. Casari and S.-Z. Qiao, *Nanoscale*, 2016, **8**, 18507-18515.
33. M. A. Sayeed, T. Herd and A. P. O'Mullane, *Journal of Materials Chemistry A*, 2016, **4**, 991-999.
34. M. A. Sayeed and A. P. O'Mullane, *Journal of Materials Chemistry A*, 2017, **5**, 23776-23784.
35. Y. Zhang, B. Cui, Z. Qin, H. Lin and J. Li, *Nanoscale*, 2013, **5**, 6826-6833.
36. C. Cai, S. Han, X. Zhang, J. Yu, X. Xiang, J. Yang, L. Qiao, X. Zu, Y. Chen and S. Li, *RSC Adv.*, 2022, **12**, 6205-6213.
37. Z. Zhuang, W. Sheng and Y. Yan, *Advanced materials*, 2014, **26**, 3950-3955.
38. B. S. Yeo and A. T. Bell, *Journal of the American Chemical Society*, 2011, **133**, 5587-5593.
39. X. Lu, Y. H. Ng and C. Zhao, *ChemSusChem*, 2014, **7**, 82-86.
40. S. Choi, S. A. Lee, J. W. Yang, W. Sohn, J. Kim, W. S. Cheon, J. Park, J. H. Cho, C. W. Lee and S. E. Jun, *Journal of Materials Chemistry A*, 2023.
41. B. Cowie, A. Tadich and L. Thomsen, 2010.
42. M. Görlin, M. Gliech, J. F. de Araújo, S. Dresp, A. Bergmann and P. Strasser, *Catalysis Today*, 2016, **262**, 65-73.
43. B. Cao, C. Luo, J. Lao, H. Chen, R. Qi, H. Lin and H. Peng, *ACS omega*, 2019, **4**, 16612-16618.
44. E. T. Bekele, H. Murthy, D. Muniswamy, Y. A. Lemenh, M. S. Shume, G. Tadesse Ayanie, A. P. Kumar, C. Ravikumar, R. Balachandran and A. Roy, *Bioinorganic Chemistry and Applications*, 2022, **2022**.
45. D. Castillo-López and U. Pal, *Journal of nanoparticle research*, 2014, **16**, 1-15.
46. G. M. Al-Senani, N. M. Deraz and O. H. Abd-Elkader, *Processes*, 2020, **8**, 844.
47. B. H. Suryanto, Y. Wang, R. K. Hocking, W. Adamson and C. Zhao, *Nature communications*, 2019, **10**, 5599.
48. H. Zhang, Y. Zhou, M. Xu, A. Chen, Z. Ni, O. Akdim, T. Wågberg, X. Huang and G. Hu, *ACS nano*, 2022, **17**, 636-647.
49. J. Yang, H. Liu, W. N. Martens and R. L. Frost, *The Journal of Physical Chemistry C*, 2010, **114**, 111-119.
50. J.-P. Sylvestre, S. Poulin, A. V. Kabashin, E. Sacher, M. Meunier and J. H. Luong, *The Journal of Physical Chemistry B*, 2004, **108**, 16864-16869.
51. F. De Groot, *Coordination Chemistry Reviews*, 2005, **249**, 31-63.
52. G. Van der Laan and I. Kirkman, *Journal of Physics: Condensed Matter*, 1992, **4**, 4189.
53. J. Van Elp, G. Peng, B. Searle, S. Mitra-Kirtley, Y. Huang, M. Johnson, Z. Zhou, M. Adams, M. Maroney and S. Cramer, *Journal of the American Chemical Society*, 1994, **116**, 1918-1923.
54. D. Bora, X. Cheng, M. Kapilashrami, P. Glans, Y. Luo and J.-H. Guo, *Journal of synchrotron radiation*, 2015, **22**, 1450-1458.
55. F. M. de Groot, J. Fuggle, B. Thole and G. Sawatzky, *Physical Review B*, 1990, **42**, 5459.
56. C.-F. Chang, Z. Hu, H. Wu, T. Burnus, N. Hollmann, M. Benomar, T. Lorenz, A. Tanaka, H.-J. Lin and H. Hsieh, *Physical review letters*, 2009, **102**, 116401.
57. J. Ludwig, C. Alarcón-Suesca, S. Geprägs, D. Nordlund, M. M. Doeff, I. P. Orench and T. Nilges, *RSC Advances*, 2017, **7**, 28069-28081.
58. H. Liu, J. Guo, Y. Yin, A. Augustsson, C. Dong, J. Nordgren, C. Chang, P. Alivisatos, G. Thornton and D. F. Ogletree, *Nano Letters*, 2007, **7**, 1919-1922.
59. G. Wan, P. Yu, H. Chen, J. Wen, C. j. Sun, H. Zhou, N. Zhang, Q. Li, W. Zhao and B. Xie, *Small*, 2018, **14**, 1704319.
60. K. Oura, V. Lifshits, A. Saranin, A. Zotov and M. Katayama, *Surface science: an introduction*, Springer Science & Business Media, 2013.
61. A. Moysiadou, S. Lee, C.-S. Hsu, H. M. Chen and X. Hu, *Journal of the American Chemical Society*, 2020, **142**, 11901-11914.
62. D. Drevon, M. Görlin, P. Chernev, L. Xi, H. Dau and K. M. Lange, *Scientific reports*, 2019, **9**, 1-11.
63. B. S. Yeo and A. T. Bell, *The Journal of Physical Chemistry C*, 2012, **116**, 8394-8400.
64. Y. Gorlin, C.-J. Chung, J. D. Benck, D. Nordlund, L. Seitz, T.-C. Weng, D. Sokaras, B. M. Clemens and T. F. Jaramillo, *Journal of the American Chemical Society*, 2014, **136**, 4920-4926.

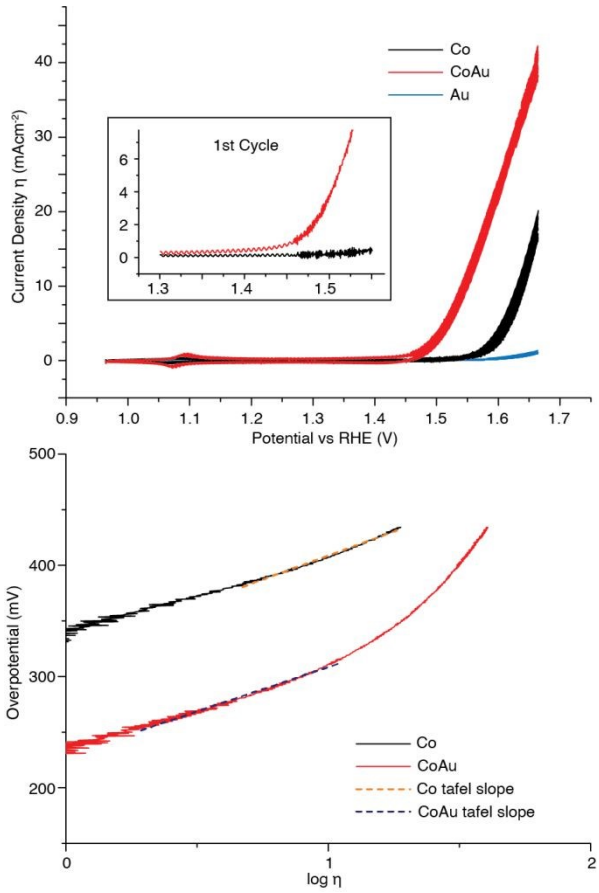

Fig. 1 (a) Cyclic voltammograms for $Co(OH)_2$ (black) and $Co(OH)_2$-Au (red) films show higher current density and earlier onset potential for the $Co(OH)_2$-Au film. The cyclic voltammogram for a pure Au film shows significantly worse performance (blue). (b) The Tafel plots for $Co(OH)_2$ (black) and $Co(OH)_2$-Au (red) films that show improved electron transfer kinetics at $Co(OH)_2$-Au.

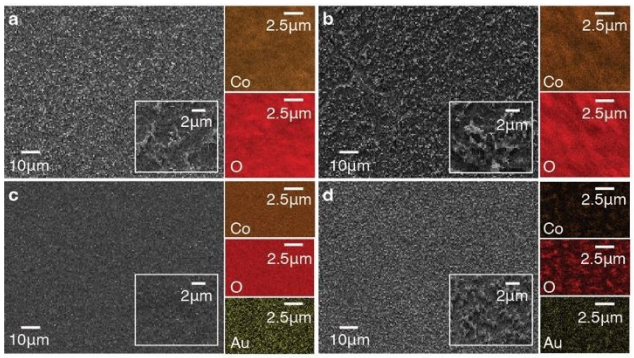

Fig. 2 SEM and EDX images of (a) $Co(OH)_2$, (b) $Co(OH)_2$ after 4 h of the OER, (c) $Co(OH)_2$-Au and (d) $Co(OH)_2$-Au after 4 h of the OER. $Co(OH)_2$ has a flake like surface while $Co(OH)_2$-Au surface appears smoother. After OER both films become coarser. EDX maps show uneven distribution of Au in $Co(OH)_2$-Au which is present in reduced agglomeration after the OER.

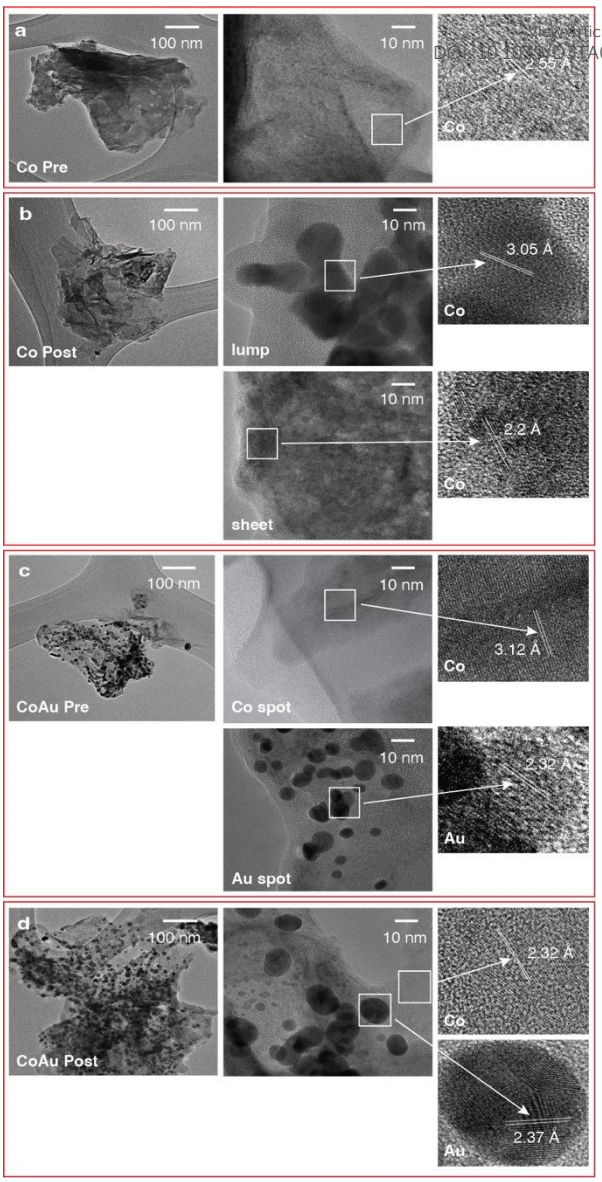

Fig. 3 TEM images of (a) $Co(OH)_2$, (b) $Co(OH)_2$ after 4 h of the OER, (c) $Co(OH)_2$-Au and (d) $Co(OH)_2$-Au after 4 h of the OER films.

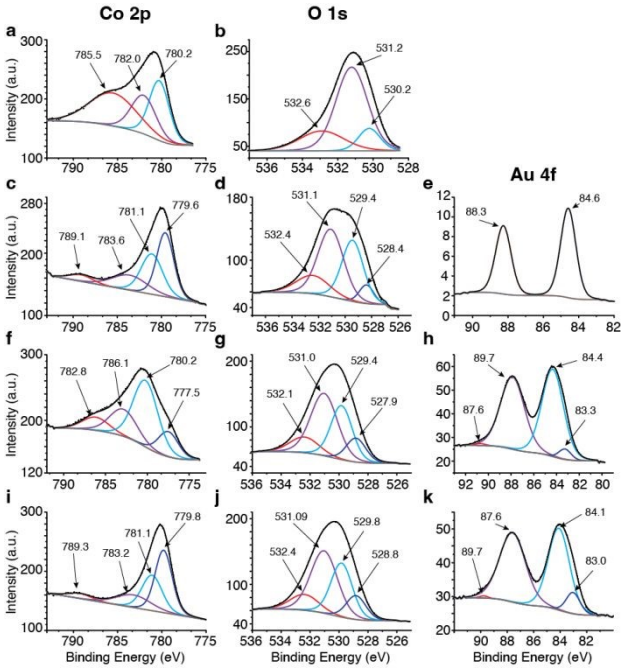

Fig. 4 XPS spectra of Co 2p, O 1s and Au 4f for (a-b) $Co(OH)_2$ (c-d) $Co(OH)_2$ post-OER (f-h) $Co(OH)_2$-Au and (i-k) $Co(OH)_2$-Au post-OER. Co 2p indicates shift to a higher oxidation state in both samples after OER while O 1s points to partial oxidation of hydroxide to lattice oxide after OER. Shoulder peaks in Au 4f indicates presence of Au presumably under a surface layer of $Co(OH)_2$. Comparison of the Au 4f XPS spectra of an Au film (e) with the $Co(OH)_2$-Au pre-OER Au 4f spectra (h) shows a shift of the main peaks to a lower energy in the $Co(OH)_2$-Au pre-OER film, indicating an electronic shift in the film as Au acts as an electron sink when Co is present.

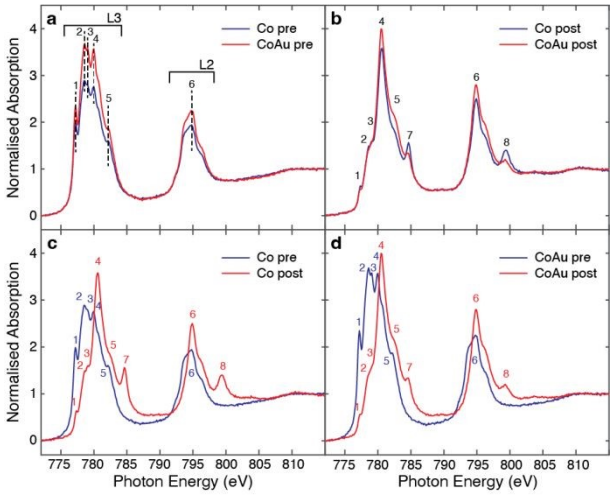

Fig. 5 NEXAFS spectra comparison in AEY mode between (a) $Co(OH)_2$ and $Co(OH)_2$-Au samples, (b) $Co(OH)_2$ and $Co(OH)_2$-Au post OER samples (c) $Co(OH)_2$ pre OER and $Co(OH)_2$ post OER samples (d) $Co(OH)_2$-Au pre- and $Co(OH)_2$-Au post-OER samples. Two regions L2 and L3 are observed from spin-orbit coupling that match the NEXAFS peaks of Co^{2+} O_h symmetry. The shift to higher energy of the post-OER spectra in both samples is due to the shift to a higher oxidation state of cobalt. Satellite peaks 7 and 8 are observed in the post-OER samples that originate from the metal-to-ligand charge transfer, but they are less prominent in the $Co(OH)_2$-Au post OER sample.

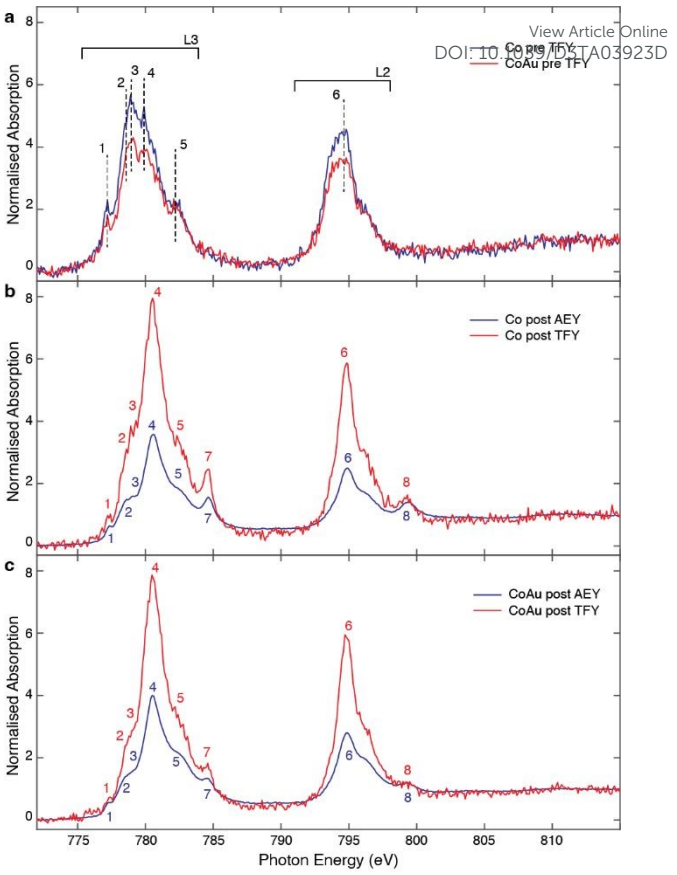

Fig. 6 NEXAFS spectra comparison between (a) Co(OH)2 and Co(OH)2-Au pre OER in TFY mode, (b) Co(OH)2 post OER AEY and TFY (c) Co(OH)2-Au post OER AEY and TFY. When the intensity of the satellite peak 7 is compared to that of the most prominent peak 4 in both AEY (blue) and TFY (red) mode, peak 7 appears less intense in TFY mode than in the AEY mode indicating that metal-to-ligand charge transfer is more of a surface phenomenon.

Journal of Material Chemistry A PAPER

View Article Online
DOI: 10.1039/D3TA03923D

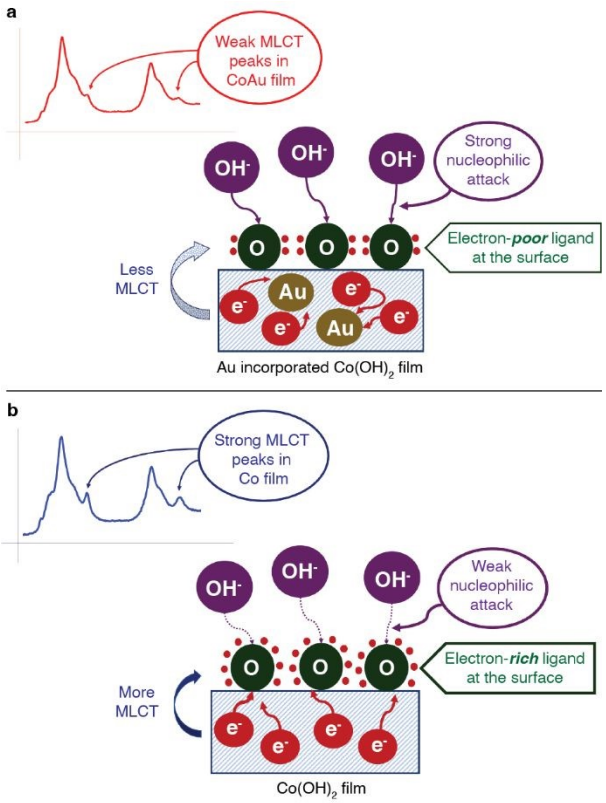

Fig. 7 Schematic of the influence of the metal-ligand-metal charge transfer effect in Au incorporated and Au free $Co(OH)_2$ based thin film electrocatalyst for the OER. The Au in the Au incorporated $Co(O H)_2$ film (a) draws the electrons due to its high electronegativity reducing metal to ligand charge transfer, thus enabling stronger nucleophilic attack on the surface ligands by the OH^- from the electrolyte while absence of Au in the Au free $Co(OH)_2$ film (b) shows no such effect on the MLCT leading to a weaker nucleophilic attack by the OH^- on the electron rich surface ligands.